PAPER

Check for updates

Efficient synthesis of tetrazoles *via* [2 + 3] cycloaddition reaction catalyzed by cobalt–nickel on magnetic mesoporous hollow spheres†

Maryam Ansari, [ID] Amir Hossein Ghasemi [ID] and Hossein Naeimi [ID] *

This study reports the fabrication and characterization of a novel magnetic Co–Ni/Fe_3O_4@mesoporous silica hollow sphere (Co–Ni/Fe_3O_4@MMSHS) nanocomposite. Then, it was used as an effective nanocatalyst to efficiently synthesize tetrazoles from various aromatic nitriles and sodium azide through a [2 + 3] cycloaddition reaction. This nanocatalyst was provided through a multi-step process involving the preparation of carbon spheres, their magnetization with Fe_3O_4, loading with cobalt and nickel nanoparticles, and subsequent silica coating and calcining to form a mesoporous hollow structure. The nanocatalyst was characterized using various techniques, including FT-IR, XRD, FE-SEM, EDS, elemental mapping, BET, and VSM, confirming its successful synthesis and desired properties. The catalytic performance of the Co–Ni/Fe_3O_4@MMSHS was evaluated for the synthesis of a range of tetrazole derivatives. The results demonstrated high catalytic activity, achieving excellent product yields (up to 98%) within short reaction times (8–44 minutes) under mild conditions. The catalyst demonstrated excellent recyclability and reusability, making it an environmentally friendly and economically viable choice for tetrazole synthesis. This study emphasizes the potential of using rationally designed nanocatalysts for efficient and sustainable organic transformations.

1. Introduction

Catalysts are substances that enhance the rate of a chemical reaction without being consumed.[1,2] Catalysts are pivotal in numerous chemical processes, significantly accelerating reaction rates that would otherwise be prohibitively slow or not occur.[3] By lowering the activation energy required for a reaction, the catalysts enhance efficiency and reduce energy consumption, thereby minimizing production costs.[4,5] Furthermore, many catalysts exhibit selectivity, enabling the targeted synthesis of desired products while suppressing the formation of undesirable byproducts.[6–8]

They play an essential role in many industrial processes, including the production of chemicals,[9–11] fuels,[12,13] and pharmaceuticals.[14,15] Also, the catalysts are crucial in reducing emissions within the automotive industry and other sectors.[16–19]

Recent advancements in nanotechnology have spurred the development of innovative catalytic materials, particularly porous[20–22] and hollow[23–26] nanostructures. These novel catalysts offer substantial advantages over their conventional counterparts.

These nanocatalysts exhibit exceptional catalytic activity due to their remarkably high surface-to-volume ratios, facilitating enhanced interaction with reactants and accelerating reaction kinetics. Moreover, the unique architectures of porous and hollow nanostructures provide precise control over reaction environments and offer a significantly increased density of active catalytic sites.[27] These distinctive properties render nanocatalysts highly promising for a wide range of applications, including energy conversion, environmental remediation, and the sustainable production of chemicals and pharmaceuticals.[28]

Hollow nanostructures are one of the new fields of research in nanosciences. These nanostructures are one of the most used organic reaction catalysts due to their unique capabilities such as; large surface area, large and adjustable internal volume, *etc*.[29] The shell of these nanostructures provides the possibility of optimizing the contact surface of the catalyst with the reactant, which, due to this unique feature, increases the efficiency of the catalyst.[30] Changing their compounds can improve catalytic activity, stability, and resistance to catalyst poisoning. One of the outstanding advantages of these structures is the ability to magnetize them. This feature allows the nanocatalyst to be easily separated from the reaction medium and recycled. In green chemistry, these nanostructures reduce the consumption of dangerous chemicals for the environment. In addition to catalysis applications, the hollow nanostructures have many applications in other fields, such as energy storage,[31] sensors,[32] and drug delivery.[33] This versatility is due to the ability to adjust their structural properties, allowing researchers to find innovative applications for these nanostructures.

Department of Organic Chemistry, Faculty of Chemistry, University of Kashan, Kashan, 87317-51167, I. R. Iran. E-mail: Naeimi@kashanu.ac.ir; Fax: +983155912397; Tel: +98-31-55912388

A diverse array of nanocatalysts exists, encompassing metallic, metal oxide, and metal–polymer hybrid materials.[34–36] Each class exhibits unique physicochemical properties, rendering them suitable for specific applications. Furthermore, incorporating multiple metals within a single catalytic system has emerged as a prominent strategy in modern catalysis. This approach, often called bimetallic or multimetallic catalysis, has significantly enhanced the efficiency of numerous organic transformations. The synergistic interactions between the different metals within these systems usually lead to dramatic improvements in catalytic activity, enabling rapid and highly efficient conversion of reactants to desired products.

Tetrazoles are aromatic heterocyclic compounds consisting of a five-membered ring containing four nitrogen atoms and one carbon atom. Due to their stability and similarity to the carboxylate group, they are used as pharmaceutical precursors to design advanced drugs. The presence of multiple nitrogens in the structure of these compounds enables them to create strong hydrogen bonds, which makes them useful in certain chemicals. In addition, tetrazoles are the precursors of many effective and valuable catalysts in the synthesis of complex materials.[37] Also, scientists have found antibacterial and anti-cancer properties in certain tetrazoles through their research.

One of the most common methods for synthesizing tetrazoles is using various nitriles in the presence of sodium azide. A common approach is [2 + 3] cycloaddition reactions using nitriles and sodium azide as raw materials. This method is popular due to its simplicity and high efficiency. Sinha et al. developed 5-substituted 1H-tetrazoles by creating a cobalt(II) complex with the tetradentate ligand N,N-bis(pyridin-2-ylmethyl)quinoline-8-amine, utilizing nitrile derivatives alongside sodium azide. They employed cobalt complexes in a [2 + 3] cycloaddition reaction to synthesize 1H-tetrazoles for the first time.[38] Safari and colleagues synthesized tetrazole derivatives from N-aryl cyanamides and sodium azide utilizing CuO–NiO–ZnO through both ultrasonic and thermal methods.[39] Acid, base, or metallic catalysts have advanced these reactions. The use of an acid catalyst, which must be a strong acid, reduces reaction time and high selectivity in product type, but one of the major problems of using strong acid is the corrosion of equipment, especially on an industrial scale. On the other hand, using strong bases as catalysts in synthetic tetrazoles is a common and compatible method with sensitive functional groups. These reactions are carried out in polar solvents, and their advantages include reducing the production of unwanted products, but one of the significant disadvantages of this method is the possibility of unwanted formation of tetrazolium salts.

Synthesizing tetrazoles with nanocatalysts presents safety, stability, efficiency, and design challenges. Addressing these challenges requires innovative strategies to create safe and appropriate nanocatalysts for industrial use. Nanocatalysts have attracted significant attention due to advantages such a high surface-to-volume ratio, easy recovery, and reusability. However, several challenges remain in the catalyzed synthesis of tetrazole derivatives via [2 + 3] cycloaddition reaction. The handling and reuse of nanocatalysts can be unstable under reaction conditions, reducing reusability and complicating the separation process.

Numerous nanocatalysts, particularly those using metal catalysts on inorganic supports, can experience desorption throughout the reaction or work-up stages. This desorption may decrease catalyst efficiency and lead to product contamination. In addition, the formation of stable metal–tetrazole complexes may complicate the separation process and impact overall efficiency. Without a suitable catalyst, the [2 + 3] cycloaddition reaction is slow and yields low amounts. Although nanocatalysts can somewhat overcome this problem, not all are equally efficient.

This research investigated the effects of a novel heterogeneous catalyst based on magnetic silica hollow spheres containing cobalt and nickel metals on the synthesis of tetrazoles from various nitrile derivatives and sodium azide. This catalyst with a unique structure has the potential to significantly improve the efficiency and speed of the reaction compared to traditional methods. The traditional synthetic methods of tetrazoles are often associated with problems such as; using harmful organic solvents, the need for harsh reaction conditions, and the production of side products. In this method, we seek to present a greener and more efficient process for synthesizing tetrazoles.

2. Experimental

2.1. Materials and apparatus

To guarantee optimal results, all reagents used in this study were of analytical grade purity and sourced from reputable chemical suppliers, Merck, Fluka, and Sigma-Aldrich. All other reagents were used without further purification. The progress of the reaction was monitored using thin-layer chromatography (TLC) with silica gel 60 F_{254} plates. The melting points of the synthesized organic compounds were analysed using a Thermo Scientific 9200 melting point apparatus. Fourier transform infrared (FT-IR) spectra were obtained using potassium bromide (KBr) pellets on a Nicolet IMPACT-400 FT-IR spectrophotometer, covering the range of 400 to 4000 cm^{-1}. ^{1}H NMR spectra were obtained using a Bruker DRX-400 spectrometer, with CDCl$_3$ as the solvent and tetramethylsilane (TMS) as the internal standard. Also, X-ray powder diffraction (XRD) patterns were obtained using a Panalytical X'Pert Pro diffractometer that utilized a Cu Kα radiation source ($\lambda = 1.54$ Å). A BELSORP-mini II device evaluated nitrogen adsorption and desorption isotherms at 77 K. The BET (Brunauer–Emmett–Teller) method calculated the specific surface area. The magnetic properties of the catalyst were evaluated at room temperature using a vibrating sample magnetometer (model VSM 7300, Meghnatis Daghigh Kavir Co., Kashan, Iran) with an applied magnetic field of 15 kOe. Finally, High-resolution imaging of the nanoparticles was performed with a Zeiss field emission scanning electron microscope (FE-SEM) set to an accelerating voltage of 15 kV.

2.2. General procedure for preparation of Co–Ni/Fe$_3$O$_4$@magnetic mesoporous silica hollow spheres (Co–Ni/Fe$_3$O$_4$@MMSHS)

First, 12 g of D-glucose was dissolved in 80 mL of deionized water to obtain a clear solution. The solution was placed in a 300 mL Teflon-lined steel autoclave and processed for 5 h at 180 °C. Once

the contents inside the Teflon-lined steel autoclave reached ambient temperature, the carbon spheres were separated using a centrifuge (5500 rpm, 5 min), washed several times with deionized water and ethanol, and dried at 50 °C for 12 h.

To prepare magnetic Fe_3O_4 nanoparticles, ultrasonic waves dissolved 9.6 g of $FeCl_3 \cdot 6H_2O$ and 4 g of $FeCl_2 \cdot 4H_2O$ well in 90 mL of deionized water. The resulting solution was transferred to a 250 mL flask equipped with an N_2 system and stirred for 30 min by a mechanical stirrer. Then, the solution temperature was raised to 90 °C, stirred for another 30 min, and then, 24 mL of 30% ammonia was added drop by drop to the solution with a syringe. After the reaction mixture was stirred for another 2 h at 90 °C, it was brought to ambient temperature, and magnetic nanoparticles were separated with the help of an external magnet and washed several times with deionized water. The obtained magnetic nanoparticles were dried for 8 h at 60 °C and stored in a sealed container for use in the following steps.

To magnetize the carbon spheres synthesized in the previous step (Fe_3O_4 to carbon spheres ratio of 1 : 1.67), place 1.2 g of Fe_3O_4 nanoparticles in 160 mL of hydrochloric acid solution (pH = 2.3). In a separate container, add 2 g of carbon spheres to 120 mL of hydrochloric acid solution (pH = 2.3). Both mixtures were exposed to ultrasound waves for 20 minutes to ensure proper dispersion. The two solutions prepared in the previous step were slowly added to each other and stirred for 6 h. Then, the magnetic carbon nanospheres were separated with an external magnet and washed well with deionized water to neutralize them. Finally, the magnetic carbon nanospheres (Fe_3O_4@carbon nanospheres) were dried at 50 °C for 12 h.

To load cobalt and nickel nanoparticles on the surface of magnetic carbon nanospheres (Co–Ni/Fe_3O_4@carbon nanospheres), 10 mg of each $CoCl_2 \cdot 6H_2O$ and $NiCl_2 \cdot 6H_2O$ salts were first dissolved in 60 mL of deionized water. The prepared solution was gradually added to 300 mg of magnetic carbon spheres suspended in 50 mL of deionized water. The resulting mixture was stirred for 10 h by a mechanical stirrer. The carbon nanospheres functionalized with nickel and cobalt were separated from the reaction medium using an external magnet, washed several times with deionized water and ethanol, and maintained at 50 °C for 12 h.

In the last step, the Co–Ni/Fe_3O_4@carbon nanospheres prepared in the previous step were dispersed in 80 mL of deionized water for 20 min with the help of ultrasonic waves. Then, 60 mL of ethanol, 2 mL of 30% ammonia, and 0.3 g of CTAB were added to the prepared solution and stirred vigorously. After 10 min, 400 μL of TEOS were added to the reaction mixture. Finally, after 8 h, the nanoparticles were separated with an external magnet and washed with water and ethanol. The nanoparticles were dried at 50 °C for 12 h. Then, the dried nanoparticles were calcined at 400 °C with a ramping rate of 2 °C per minute for 7 h in an air atmosphere to obtain the Co–Ni/Fe_3O_4@MMSHS.

2.3. General procedure for the synthesis of tetrazole derivatives

A 25 mL round-bottom flask equipped with a magnetic stirrer was set up with the following reagents: 1.2 mmol of sodium azide, 1 mmol of an aromatic nitrile, 8 mg of Co–Ni/Fe_3O_4@-MMSHS as a catalyst, and 5 mL of H_2O/EtOH (1 : 1) as the solvent. The reaction mixture was heated at 60 °C for the time indicated in Table 4. The progress of the reaction was monitored using thin-layer chromatography (TLC). Once the reaction was complete, the container's contents were cooled to room temperature, and the magnetic catalyst was separated from the reaction environment using an external magnet. The separated catalyst was washed several times with distilled water and methanol and then dried at 50 °C (6 h) for reuse. The resulting sediments were separated from the reaction medium using filter paper. 20 mL of 5 N HCl and 20 mL of ethyl acetate were added to the filtered solution. The organic phase was separated, dried over anhydrous $MgSO_4$, and concentrated under reduced pressure. The crude product was purified through recrystallization from ethanol to obtain the pure product. All products were confirmed by their melting points and spectroscopic methods, such as FT-IR and ^{1}H NMR.

2.3.1 Spectroscopic and physical data

2.3.1.1 5-(4-Nitrophenyl)-2H-tetrazole (3a). Cream solid; m.p.: 218–220 °C (Lit. m.p.: 218–220 °C);[40] FT-IR (KBr): ν = 3447, 2917, 2852, 1608, 1487, 1441, 1133, 1086, 994 cm^{-1}; ^{1}H NMR (400 MHz, DMSO-d$_6$) δ (ppm): 8.30 (d, 2H, J = 8.0 Hz), 8.45 (d, 2H, J = 8.0 Hz).

2.3.1.2 5-(4-Fluorophenyl)-2H-tetrazole (3b). White solid; m.p.: 209–210 °C (Lit. m.p.: 210–211 °C);[41] FT-IR (KBr): ν = 3435, 3075, 2851, 1611, 1446, 1412, 1164, 1051, 989 cm^{-1}; ^{1}H NMR (400 MHz, DMSO-d$_6$) δ (ppm): 7.45 (d, 2H, J = 8.0 Hz), 8.07 (d, 2H, J = 8.0 Hz), 16.90 (s, NH).

2.3.1.3 5-(4-Bromophenyl)-2H-tetrazole (3c). Cream solid; m.p.: 263–265 °C (Lit. m.p.: 263–266 °C);[40] FT-IR (KBr): ν = 3435, 3002, 2768, 1605, 1482, 1430, 1156, 1075, 1055, 832 cm^{-1}; ^{1}H NMR (400 MHz, DMSO-d$_6$) δ (ppm): 7.45 (d, 2H, J = 8.0 Hz), 8.07 (d, 2H, J = 8.0 Hz), 16.90 (s, NH).

2.3.1.4 5-(4-Chlorophenyl)-2H-tetrazole (3d). Cream solid; m.p.: 260–264 °C (Lit. m.p.: 262–265 °C);[40] FT-IR (KBr): ν = 3451, 2769, 1609, 1487, 1435, 1160, 1054, 834 cm^{-1}; ^{1}H NMR (400 MHz, DMSO-d$_6$) δ (ppm): 7.69 (d, 2H, J = 8.0 Hz), 8.04 (d, 2H, J = 8.0 Hz), 17.03 (s, NH).

2.3.1.5 5-(4-Methylphenyl)-2H-tetrazole (3e). Cream solid; m.p.: 248–250 °C (Lit. m.p.: 248–250 °C);[42] FT-IR (KBr): ν = 3435, 3045, 2918, 2769, 1615, 1436, 1405, 1163, 1084, 1053, 990 cm^{-1}; ^{1}H NMR (400 MHz, DMSO-d$_6$) δ (ppm): 2.38 (s, 3H, J = 8.0 Hz), 7.41 (d, 2H, J = 8.0 Hz), 7.92 (d, 2H, J = 8.0 Hz), 16.76 (s, NH).

2.3.1.6 5-(2-Fluorophenyl)-2H-tetrazole (3f). White solid; m.p.: 161–163 °C (Lit. m.p.: 161–162 °C);[43] FT-IR (KBr): ν = 3436, 2986, 2761, 1620, 1490, 1456, 1152, 1109, 1059, 995 cm^{-1}; ^{1}H NMR (400 MHz, DMSO-d$_6$) δ (ppm): 7.44 (t, 1H, J = 8.0 Hz), 7.49 (t, 1H, J = 8.0 Hz), 7.64–7.69 (m, 1H), 8.05 (t, 1H, J = 8.0 Hz), 16.86 (s, NH).

2.3.1.7 5-(3-Nitrophenyl)-2H-tetrazole (3g). Cream solid; m.p.: 155–156 °C (Lit. m.p.: 154–156 °C);[40] FT-IR (KBr): ν = 3304, 3089, 2896, 2749, 1621, 1528, 1471, 1157, 1078, 1021, 870 cm^{-1}; ^{1}H NMR (400 MHz, DMSO-d$_6$) δ (ppm): 7.82–7.91 (d, 1H, J = 8.0 Hz), 8.41 (d, 1H, J = 8.0 Hz), 8.45 (d, 1H, J = 8.0 Hz), 8.82 (s, 1H), 16.81 (s, NH).

2.3.1.8 5-(3-Methylphenyl)-2H-tetrazole (3h). Yellow solid; m.p.: 249–251 °C (Lit. m.p.: 249–251 °C);[44] FT-IR (KBr): $\nu = 3433$, 2888, 1599, 1566, 1470, 1439, 1412, 1393, 1050, 745 cm^{-1}; ^{1}H NMR (400 MHz, DMSO-d$_6$) δ (ppm): 7.39 (d, 1H, $J = 8.0$ Hz), 7.47–7.49 (d, 1H, $J = 8.0$ Hz), 7.82 (d, 1H, $J = 8.0$ Hz), 7.86 (s, 1H), 16.81 (s, NH).

2.3.1.9 5-(2-Methylphenyl)-2H-tetrazole (3i). Yellow solid; m.p.: 230–233 °C (Lit. m.p.: 232–233 °C);[45] FT-IR (KBr): $\nu = 3431$, 2980, 1618, 1597, 1564, 1485, 1462, 1282, 1062, 1036, 995 cm^{-1}; ^{1}H NMR (400 MHz, DMSO-d$_6$) δ (ppm): 7.39 (d, 1H, $J = 8.0$ Hz), 7.47–7.49 (d, 1H, $J = 8.0$ Hz), 7.82 (d, 1H, $J = 8.0$ Hz), 7.86 (s, 1H), 16.81 (s, NH).

2.3.1.10 2-(1H-Tetrazol-5-yl) benzonitrile (3j). White solid; m.p.: 231–232 °C (Lit. m.p.: 230–232 °C);[46] FT-IR (KBr): $\nu = 3427$, 3025, 2917, 1608, 1574, 1491, 1452, 1407, 1281, 1064, 1011, 782 cm^{-1}; ^{1}H NMR (400 MHz, DMSO-d$_6$) δ (ppm): 7.77–7.79 (t, 2H, $J = 8.0$ Hz), 7.92–7.94 (t, 2H, $J = 8.0$ Hz), 8.07–8.09 (t, 2H, $J = 8.0$ Hz).

2.3.1.11 5-(3-Bromoophenyl)-2H-tetrazole (3k). White solid; m.p.: 149–151 °C (Lit. m.p.: 149–150 °C);[42] FT-IR (KBr): $\nu = 3088$, 2747, 1621, 1528, 1471, 1412, 1350, 1077, 729 cm^{-1}; ^{1}H NMR (400 MHz, DMSO-d$_6$) δ (ppm): 7.89–7.91 (t, 2H, $J = 8.0$ Hz), 8.41 (d, 2H, $J = 8.0$ Hz), 8.47 (s, 2H), 8.83 (s, NH).

2.3.1.12 5-(4-Hydroxyphenyl)-2H-tetrazole (3l). White solid; m.p.: 230–233 °C (Lit. m.p.: 230–233 °C);[40] FT-IR (KBr): $\nu = 3430$, 2936, 1612, 1512, 1470, 1414, 1279, 1079, 791 cm^{-1}; ^{1}H NMR (400 MHz, DMSO-d$_6$) δ (ppm): 6.94 (d, 2H, $J = 8.0$ Hz), 7.85 (d, 2H, $J = 8.0$ Hz), 10.17 (s, 1H), 16.48 (s, NH).

2.3.1.13 5-Phenyl-1H-tetrazole (3m). White solid; m.p.: 230–234 °C (Lit. m.p.: 230–233 °C);[40] FT-IR (KBr): $\nu = 3432$, 3055, 2839, 1608, 1563, 1464, 1409, 1286, 1056, 726 cm^{-1}; ^{1}H NMR (400 MHz, DMSO-d$_6$) δ (ppm): 7.59–7.62 (m, 3H), 8.03 (d, 2H, $J = 8.0$ Hz), 16.85 (s, NH).

2.3.1.14 5-(4-Methoxyphenyl)-2H-tetrazole (3n). White solid; m.p.: 68–69 °C (Lit. m.p.: 68–69 °C);[47] FT-IR (KBr): $\nu = 3088$, 2747, 1621, 1528, 1471, 1350, 1077, 729 cm^{-1}; ^{1}H NMR (400 MHz, DMSO-d$_6$) δ (ppm): 3.38 (s, 3H), 7.15 (d, 2H, $J = 8.0$ Hz), 7.97 (d, 2H, $J = 8.0$ Hz), 16.63 (s, NH).

3. Results and discussion

3.1. Preparation and characterization of the catalyst

The designed catalyst was prepared in five main steps, as shown in Fig. 1. In the first stage, carbon spheres of the same shape and size were prepared using the hydrothermal method. In the next step, the carbon spheres were magnetized by Fe$_3$O$_4$. Then, cobalt and nickel metals were adsorbed on the surface of magnetic carbon spheres. These metals are the active sites in the catalytic reaction for synthesizing tetrazoles. In the third step, the silicate template and CTAB are placed on the surface of the Co–Ni/Fe$_3$O$_4$@carbon spheres. The CTAB undergoes calcination, forming pores within the catalyst structure. Finally, the prepared structure is calcined in the last stage, and the internal carbon structure is decomposed and removed. The surfactant in the silicate structural wall decomposes, forming a hollow, porous silica sphere.

The FT-IR spectra of the various stages of Co–Ni/Fe$_3$O$_4$@-MMSHS nanocatalyst preparation is presented in Fig. 2. Fig. 2a displays the spectrum of the carbon spheres formed during the glucose polymerization process. The peak observed at 3441 cm^{-1} corresponds to the stretching vibration of the O–H bond, attributed to alcoholic groups in the carbon sphere structure. The absorption peaks observed in regions 2923 and 2871 cm^{-1} are related to the asymmetric stretching and symmetric stretching vibrations of C–H sp^3 bonds, respectively. The absorption peak observed at 1712 cm^{-1} is associated with the stretching vibration of the ketone carbonyl group within the polymerized structure of glucose. The absorption peaks observed at 1627 and 1383 cm^{-1} are related to the aromatic rings formed during polymerization. The peak observed at approximately 1300 cm^{-1} is associated with the C–O stretching vibrations. Fig. 2b displays the spectrum of magnetic carbon spheres. It reveals absorption peaks at 534 and 451 cm^{-1}, which are associated with the stretching vibrations of the Fe–O bond. This evidence confirms the binding of Fe$_3$O$_4$ nanoparticles to the surface of the carbon spheres.

The absorption spectrum shown in Fig. 2c corresponds to the magnetic carbon sphere covered by cobalt and nickel. The absorption peaks observed at 593 and 470 cm^{-1} are related to Co–O and Ni–O, respectively. The increase in the intensity of the peaks associated with stretching vibrations of C–H sp^3 in the region of 2918 and 2852 cm^{-1} is due to the presence of the carbon chain of CTAB as a surfactant in the structure of the nanocatalyst (Fig. 2d). Absorption peaks at 1071 and 964 cm^{-1} correspond to the Si–O–Si and Si–OH, respectively. These peaks indicated that the SiO$_2$ is present on the surface of the nanocatalyst.

Finally, Fig. 2e displays the spectrum of the nanocatalyst following the calcination process. In this spectrum, all peaks associated with the organic substances from the previous stage
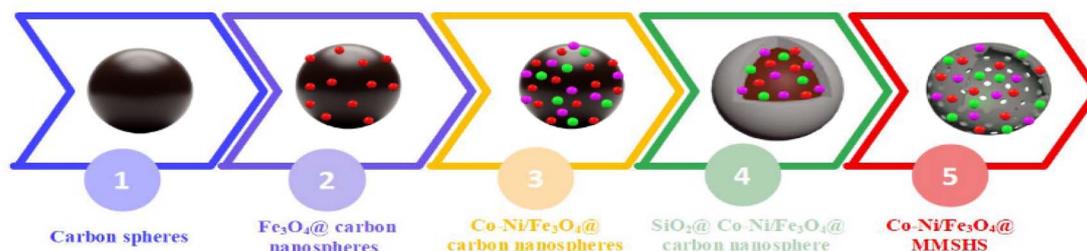
Fig. 1 Preparation steps of Co–Ni/Fe$_3$O$_4$@MMSHS nanocatalyst.

1. Carbon spheres
2. Fe$_3$O$_4$@ carbon nanospheres
3. Co-Ni/Fe$_3$O$_4$@ carbon nanospheres
4. SiO$_2$@ Co-Ni/Fe$_3$O$_4$@ carbon nanosphere
5. Co-Ni/Fe$_3$O$_4$@ MMSHS

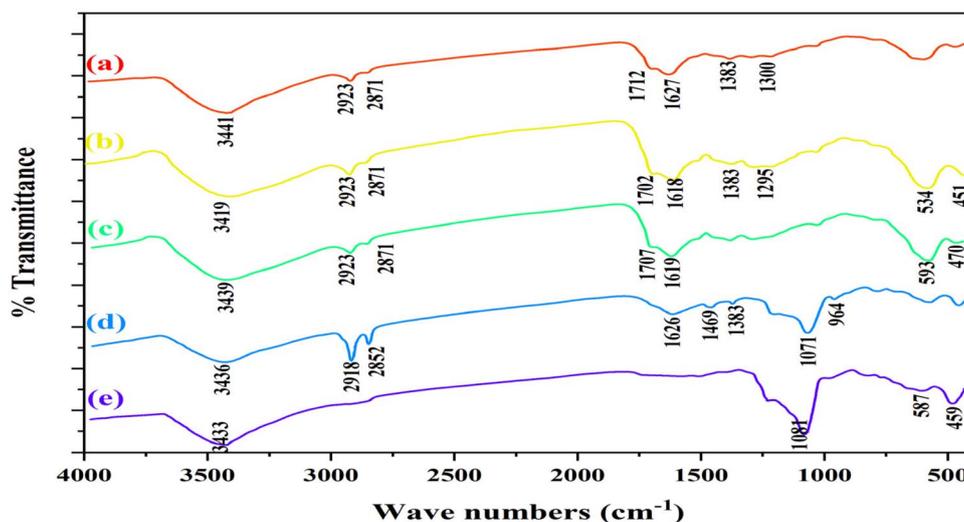**Fig. 2** The FT-IR spectra of carbon spheres (a), Fe_3O_4@carbon nanospheres (b), Co−Ni/Fe_3O_4@carbon nanospheres (c), SiO_2@Co−Ni/Fe_3O_4@carbon nanosphere (d), Co−Ni/Fe_3O_4@MMSHS (e).

have vanished, indicating their decomposition and the successful synthesis of a hollow structure.

X-ray diffraction (XRD) was utilized to investigate the different stages of the nanocatalyst synthetic process, as shown in Fig. 3. The amorphous pattern observed in the X-ray diffraction of the synthesized carbon spheres, as shown in Fig. 3a, indicates the nature of their carbon structure. Fig. 3b shows the X-ray diffraction pattern of carbon spheres after magnetization. The decrease in the pattern's height at $2\theta = 25°$ is attributed to the surface of the carbon spheres covered by

Fe_3O_4 nanoparticles. The observed pattern aligns perfectly with the pattern associated with Fe_3O_4 (JCPDS no. 01-075-0449). Additionally, the size of the Fe_3O_4 nanoparticles on the catalyst surface was determined to be 16.70 nm using the Debye–Scherrer equation. By adding cobalt and nickel to the surface of magnetic carbon spheres, the amorphous pattern seen in Fig. 3c has been eliminated due to increased structural crystallinity. According to JCPDS no. 01-086-2267 and 00-022-1086, the presence of cobalt and nickel nanoparticles in the structure has been confirmed. The pattern in Fig. 3d relates to the
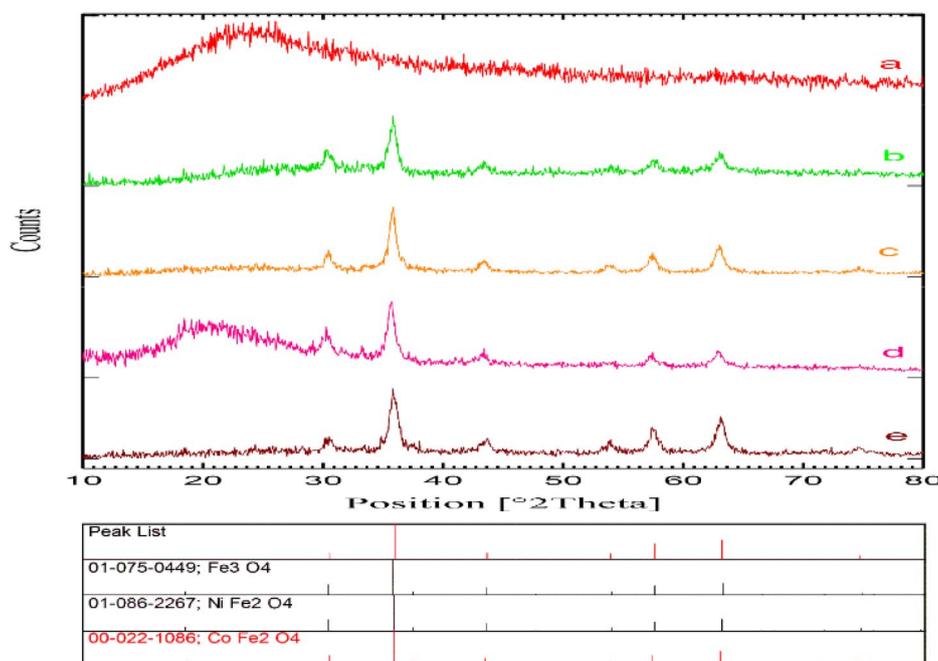
Fig. 3 The XRD patterns of carbon spheres (a), Fe_3O_4@carbon nanospheres (b), Co−Ni/Fe_3O_4@carbon nanospheres (c), SiO_2@Co−Ni/Fe_3O_4@carbon nanosphere (d), Co−Ni/Fe_3O_4@MMSHS (e).

RSC Advances Paper

nanocatalyst's silica coating. The amorphous pattern observed in $2\theta = 25°$ indicates that silica successfully covers the surface and confirms the coating process. The pattern shown in Fig. 3e illustrates the nanocatalyst after calcination. As the carbon structure and the surfactant within the silica wall of the nanocatalyst are eliminated, the crystallinity of the material increases. Consequently, the amorphous pattern observed in the previous step has disappeared. The average size of the Co–Ni/Fe$_3$O$_4$@MMSHS nanocatalyst was calculated using the Debye–Scherrer formula, with an average crystallite size of 12.31 nm.

The field emission scanning electron microscopy (FE-SEM) images of the nanocatalyst are shown at two different scales: 200 and 500 nm, illustrated in Fig. 4a and b. These images reveal the catalyst's spherical morphology. Fig. 4b demonstrates the hollowness of the Co–Ni/Fe$_3$O$_4$@MMSHS nanocatalyst. The internal space increases the contact surface between the nanocatalyst and the reactants, thereby enhancing reaction efficiency and reducing reaction time. The thickness of the nanocatalyst's silica wall was measured at 81 nm (Fig. 4b). This thickness enhances the nanocatalyst's physical and chemical resistance, allowing for consecutive reuse.

Fig. 5 illustrates the histogram displaying the size distribution of the Co–Ni/Fe$_3$O$_4$@MMSHS nanocatalyst. The mean size of the Co–Ni/Fe$_3$O$_4$@MMSHS was determined to be 388 nm, with a standard deviation of 95.05 nm.

Fig. 6 shows the energy dispersive X-ray analysis of Co–Ni/Fe$_3$O$_4$@MMSHS nanocatalyst. 12.07% of carbon was observed in the sample, which can be attributed to the residual carbon after calcination. The estimated amount of Si in the walls of nanoparticles is 14.52 wt%. Additionally, the weight percentages of Fe, Co, and Ni were measured as 22.32%, 0.39%, and 0.12%, respectively. Approximately 50.58% of the sample's weight consists of oxygen.

EDS elemental mapping analysis is a valuable method for studying the distribution of elements in nanomaterials. Fig. 7 shows the EDS elemental mapping of the Co–Ni/
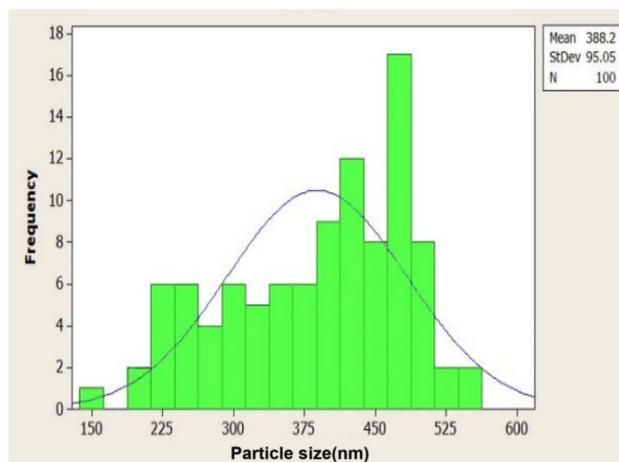

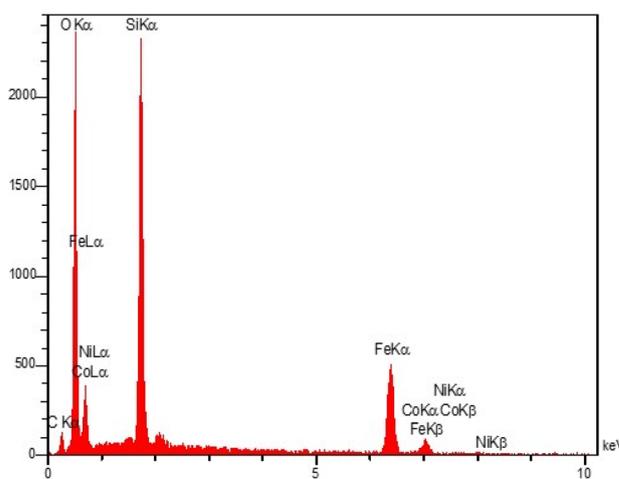Fig. 5 The histogram of the size distribution of Co–Ni/Fe$_3$O$_4$@MMSHS nanocatalyst.

Fig. 6 The energy dispersive X-ray analysis (EDX) of Co–Ni/Fe$_3$O$_4$@MMSHS nanocatalyst.
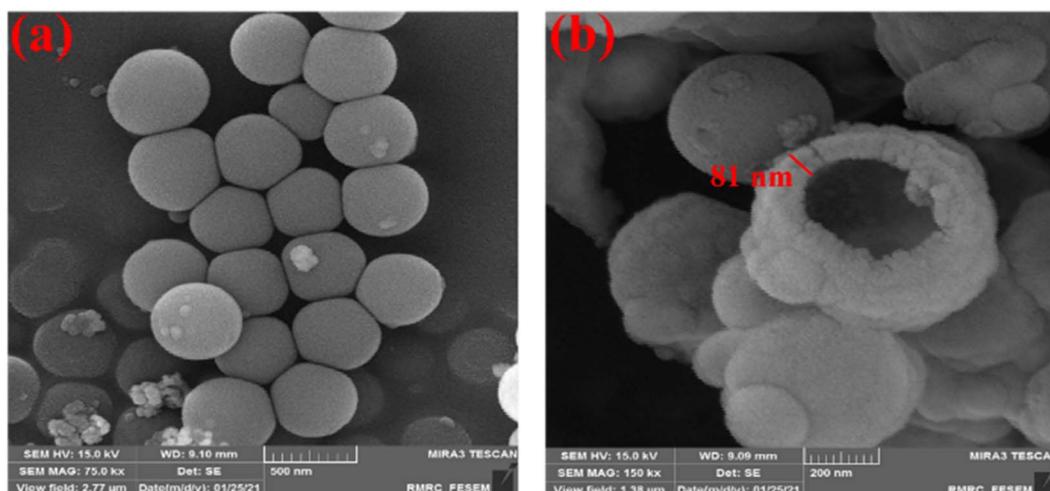

Fig. 4 The FE-SEM images of the Co–Ni/Fe$_3$O$_4$@MMSHS nanocatalyst with magnification 500 (a) and 200 (b) nanometers.
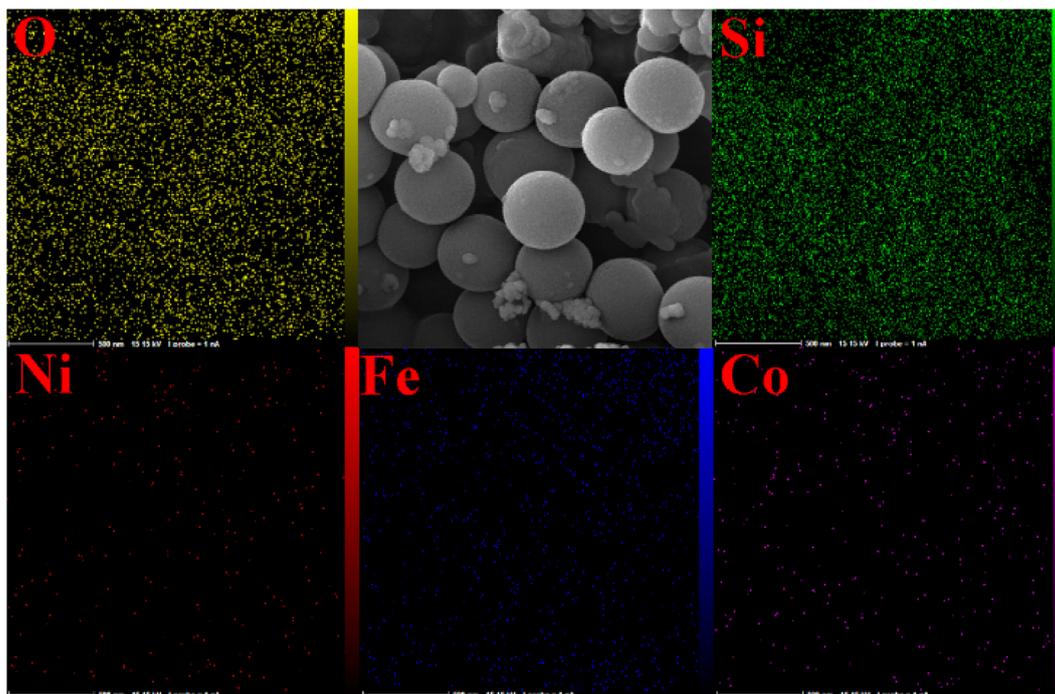
Fig. 7 The EDS elemental mapping of the Co−Ni/Fe$_3$O$_4$@MMSHS nanocatalyst.

Fe$_3$O$_4$@MMSHS nanocatalyst. The obtained data show the proper dispersion of O, Ni, Si, Co, Fe elements throughout the nanocatalyst. The uniform dispersion of nanoparticles as catalytic active sites enhances nanocatalyst efficiency, ensuring uniform catalytic performance across the entire surface.

The Brunauer–Emmett–Teller (BET) technique estimates the surface area, pore volume, and pore size of the Co–Ni/Fe$_3$-O$_4$@MMSHS nanocatalyst (Fig. 8). The BET plot (Fig. 8a) indicates that the nanocatalyst's specific surface area is 204.83 m^2 g^{-1}. Additionally, this technique calculates the total pore volume of the Co-nanocatalyst, which is 0.1434 cm^3 g^{-1}.

Fig. 8b illustrates the N$_2$ adsorption–desorption isotherm for the Co–Ni/Fe$_3$O$_4$@MMSHS nanocatalyst. According to the IUPAC classification, the nanocatalyst exhibited type IV adsorption–desorption isotherms. This type of isotherm indicates the synthesized nanocatalyst is mesoporous. The

hysteresis type of the nanocatalyst is H4, commonly found in nanomaterials with inner space, like hollow spheres with mesoporous silica walls. Using the Barrett–Joyner–Halenda (BJH) method, the pore radius was determined to be 1.21 nm, and the pore area was calculated to be 18.68 m^2 g^{-1} (Fig. 8c).

Fig. 9 shows that the magnetic properties of the prepared nanoparticles are measured using the vibrating-sample magnetometry (VSM) analysis at room temperature. The magnetic property of the Fe$_3$O$_4$ nanoparticles 63.60 emu g^{-1} was measured (Fig. 9a). After layering various materials on the nanocatalyst and calcining it, the magnetic properties of the final nanocatalyst, 24.51 emu g^{-1} were measured (Fig. 9a). The analysis results indicate that the synthesized nanocatalyst retains its magnetic properties and can be easily separated from the reaction medium using an external magnet.
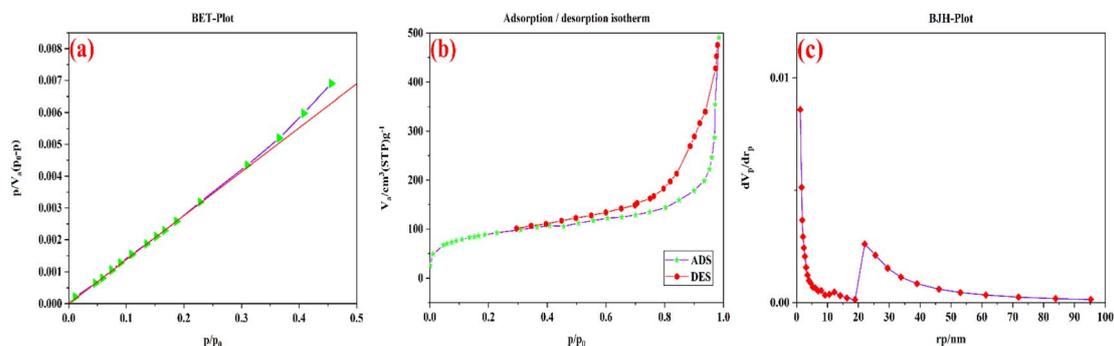

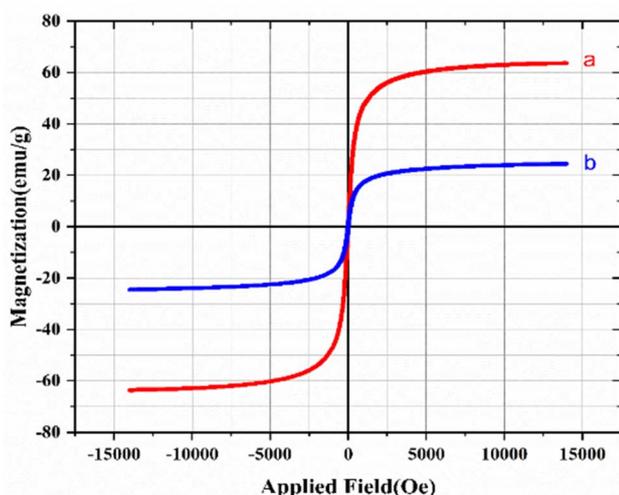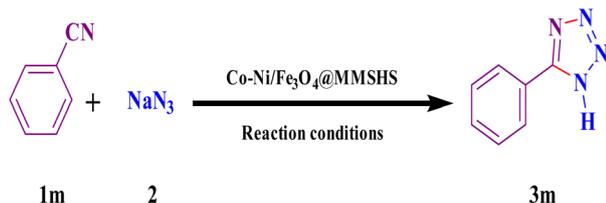**Fig. 8** The BET plot (a), adsorption/desorption isotherm (b), and BJH plot (c) of the Co−Ni/Fe$_3$O$_4$@MMSHS nanocatalyst.

Fig. 9 The VSM analysis of the Fe_3O_4 nanoparticle (a) and Co–Ni/Fe_3O_4@MMSHS nanocatalyst (b).

Scheme 1 Synthesis of 5-phenyl-1*H*-tetrazole using Co–Ni/Fe_3O_4@MMSHS nanocatalyst.

3.2. Evaluation of catalytic activity

The reaction between benzonitrile and sodium azide for synthesizing 5-phenyl-1*H*-tetrazole (**3m**) was selected as a model reaction to optimize the reaction conditions after preparing and identifying the nanocatalyst (Scheme 1). The temperature, amount of catalyst, and solvent were selected as variable factors to optimize the reaction conditions.

Table 1 shows the results of the optimum amount of catalyst. According to the obtained results, the optimal amount of catalyst is 8 mg (entry 5), and no change in reaction time or

Table 1 Optimization of catalyst amount for the synthesis of 5-phenyl-1*H*-tetrazole (**3m**)[a]

Entry	Catalyst amount (g)	Time (min)	Yield[b] (%)
1	—	300	Trace
2	0.002	240	37
3	0.004	90	66
4	0.006	32	79
5	0.008	12	98
6	0.010	12	98

[a] Reaction conditions: benzonitrile (1 mmol), sodium azide (1.2 mmol), Co–Ni/Fe_3O_4@MMSHS as a catalyst, and 5 mL of H_2O/EtOH (1 : 1) as the solvent at 60 °C. [b] Isolated yields.

Table 2 Optimization of temperature for the synthesis of 5-phenyl-1*H*-tetrazole (**3m**)[a]

Entry	Temperature	Time (min)	Yield[b] (%)
1	R.T.	300	Trace
2	40	55	77
3	60	12	98
4	80	12	98
5	100	12	98

[a] Reaction conditions: benzonitrile (1 mmol), sodium azide (1.2 mmol), Co–Ni/Fe_3O_4@MMSHS (8 mg) as a catalyst, and 5 mL of H_2O/EtOH (1 : 1) as the solvent. [b] Isolated yields.

Table 3 Optimization of the solvent for the synthesis of 5-phenyl-1*H*-tetrazole (**3m**)[a]

Entry	Solvent	Time (min)	Yield[b] (%)
1	DMSO	68	72
2	DMF	56	64
3	EtOH	188	69
4	H_2O	260	55
5	THF	260	28
6	PEG	240	56
7	Toluene	300	42
8	CH_3CN	300	17
9	H_2O/EtOH (1 : 1)	12	98

[a] Reaction conditions: benzonitrile (1 mmol), sodium azide (1.2 mmol), Co–Ni/Fe_3O_4@MMSHS (8 mg) as a catalyst, and 5 mL of selected solvent at 60 °C. [b] Isolated yields.

efficiency has been observed in higher amounts of catalyst (entry 6).

Table 2 indicates that the reaction efficiency at room temperature was very low during the temperature optimization study. By increasing the reaction temperature to 60 °C, we have seen an increase in the reaction efficiency. As a result, the catalyst has reduced the energy required to carry out the reaction. Also, no change in product yield was observed by further increasing the reaction temperature to 100 °C.
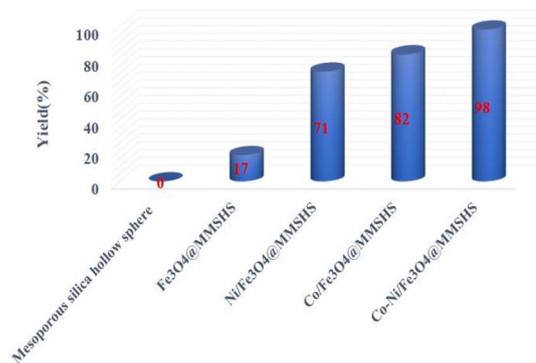

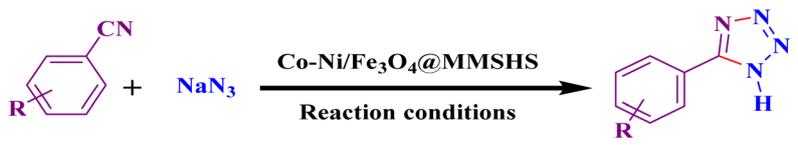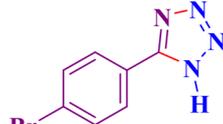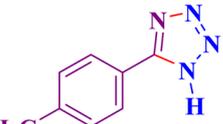**Fig. 10** Investigating the synergistic effect of the catalyst for the synthesis of the model reaction.

Table 3 shows the results of optimizing the solvent in the reaction. The solvents such as; DMSO, DMF, EtOH, H_2O, THF, PEG, toluene, CH_3CN, and H_2O/EtOH were investigated, and according to the obtained results, the 1 : 1 mixture of H_2O and EtOH showed the highest efficiency and the shortest reaction time (Table 3, entry 9).

To demonstrate the positive synergistic effect of nanoparticles in the nanocatalyst structure, the model reaction was conducted under optimal conditions using the nanoparticles illustrated in Fig. 10. According to the results obtained from Fig. 10, the mesoporous silica hollow sphere did not show the catalytic effect. The Fe_3O_4@MMSHS catalyzed the reaction due to the presence of Fe_3O_4 nanoparticles as a Lewis acid, which showed a product yield of about 17%. When nickel and cobalt nanoparticles are present individually on the surface of the magnetic hollow mesoporous spheres, lower efficiency is

Table 4 Synthesized tetrazole derivatives[a,b] from sodium azide and various aromatic nitriles

3a-n[a], Yield[b] (%), Time (min), TON, TOF (m^{-1})

3a, 93, 32, 3000, 94

3b, 95, 18, 3064, 170

3c, 95, 22, 3064, 139
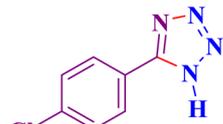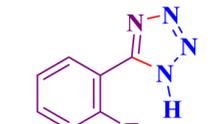
3d, 96, 28, 3096, 111

3e, 98, 8, 3161, 395

3f, 93, 21, 3000, 143
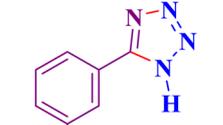
3g, 94, 38, 3032, 80

3h, 97, 10, 3129, 313

3i, 95, 15, 3064, 204
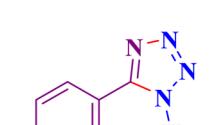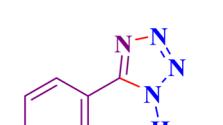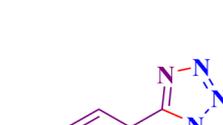
3j, 88, 44, 2838, 65

3k, 97, 25, 3129, 125

3l, 97, 8, 3129, 391
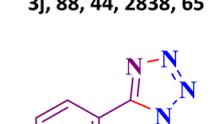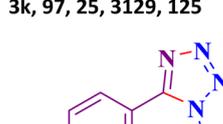
3m, 98, 12, 3161, 263

3n, 98, 6, 3161, 527

[a] Reaction conditions: 1.2 mmol of sodium azide, 1 mmol of an aromatic nitrile, 8 mg of Co–Ni/Fe_3O_4@MMSHS as a catalyst, and 5 mL of H_2O/EtOH (1 : 1) as the solvent at 60 °C. [b] Isolated yield.
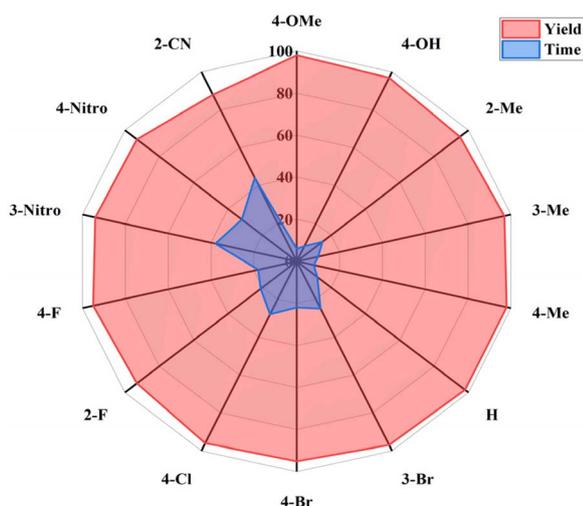
Fig. 11 Radar chart comparing efficiency and reaction time based on various substitutions.

observed compared to when both metals are present simultaneously on the surface of the nanocatalyst. This analysis demonstrated a positive synergistic effect between cobalt and nickel nanoparticles in synthesizing tetrazole derivatives.

After optimizing the reaction conditions, Table 4 shows the results of synthesizing tetrazole derivatives from various aromatic nitriles and sodium azide. This table displays each synthesized derivative's reaction time and yield under optimal reaction conditions.

The radar chart comparing yield and reaction time based on various substitutions is extracted from Table 4 and shown in Fig. 11. The results indicate that the reaction yield ranged from 88% to 98%. It was also observed that the nitrile compounds with electron-donating groups had higher yields, but they did not differ much from nitriles with electron-withdrawing groups. In addition, the results showed that nitriles with the group in position 2 have lower yield and longer time due to the steric hindrance.

Table 5 compares the Co–Ni/Fe$_3$O$_4$@MMSHS nanocatalyst with other reported catalysts for synthesizing 5-phenyl-1H-tetrazole (**3m**) from benzonitrile and sodium azide. The reactions in entries 1 to 4 were performed at temperatures above 100 °C.

The catalysts listed in this table (entries 1 to 5) are organometallic complexes, and their efficiency may decrease after multiple recoveries. Also, the solvents used in entries 1 to 4 are not green and environmentally friendly conditions. As a result, the Co–Ni/Fe$_3$O$_4$@MMSHS nanocatalyst synthesizes tetrazole derivatives with high efficiency in a shorter reaction time (Table 5, entry 6). In addition, water and ethanol solvents, which are green and environmentally friendly solvents, are used. Compared to others, one important feature of this catalyst is its high stability and reusability. All of these features have made the Co–Ni/Fe$_3$O$_4$@MMSHS nanocatalyst significantly better than the catalysts that have been previously reported.

3.3. Proposed reaction mechanism

Scheme 2 illustrates the proposed[52] the mechanism for synthesizing tetrazole derivatives from benzonitrile and sodium azide using Co–Ni/Fe$_3$O$_4$@MMSHS as a catalyst. Sodium azide first forms a complex with metals on the catalyst surface (**I**). The aromatic nitrile compound adsorbs onto the catalyst surface with nitrogen, and after the proper orientation of the reactants, a [2 + 3] cycloaddition occurs (**II**). The correct alignment of the raw materials and the complex formed on the catalyst's surface has increased the speed of the reaction. The [2 + 3] cycloaddition reaction occurs simultaneously, forming intermediate (**III**) through the creation of new bonds. After the proteolysis of intermediate **III**, the tetrazole as a final product is formed, and the catalyst reenters the reaction cycle.

3.4. Reusability

Due to the importance of catalyst recovery and environmental concerns, the designed catalyst was thoroughly investigated. The catalyst was used and recovered in several stages; its results are shown in Fig. 12. This test utilized the model reaction to evaluate the catalyst's recovery properties. After each recovery, the catalyst was washed multiple times with distilled water and methanol and dried at 50 °C for 6 h. According to the results presented in Fig. 12, after numerous recovery cycles, the catalyst exhibited only a 5% decrease in performance.

After recovery, the FE-SEM image (Fig. 13a) and XRD image (Fig. 13b) of the Co–Ni/Fe$_3$O$_4$@MMSHS show no significant changes in the catalyst's structure and morphology. After multiple recovery steps, the catalyst's structural stability

Table 5 Comparison of the catalytic activity of the Co–Ni/Fe$_3$O$_4$@MMSHS nanocatalyst with the other reported catalysts for the synthesis of 5-phenyl-1H-tetrazole (**3m**)

Entry	Catalyst (conditions)	Time (min)	Yield[a] (%)	Ref.
1	Sm-TADDbBP@MCM-41 (50 mg, PEG-400, 120 °C)	70	97	48
2	Nd-bis(PYT)@boehmite NPs (50 mg, PEG-400, 120 °C)	150	97	49
3	Cobalt(II) complex with (*N*,*N*-bis pyridin-2-yl methyl)quinolin-8-amine (1 mol%, DMSO, 110 °C)	720	99	38
4	[Cu(L)]·0.5H$_2$O (0.7 mol%, DMSO, 110 °C)	240	96	50
5	FeTSPP (0.05 mmol, H$_2$O/EtOH, 60 °C)	20	97	51
6	Co–Ni/Fe$_3$O$_4$@MMSHS (8 mg, H$_2$O/EtOH, 60 °C)	12	98	This work

[a] Isolated yield.
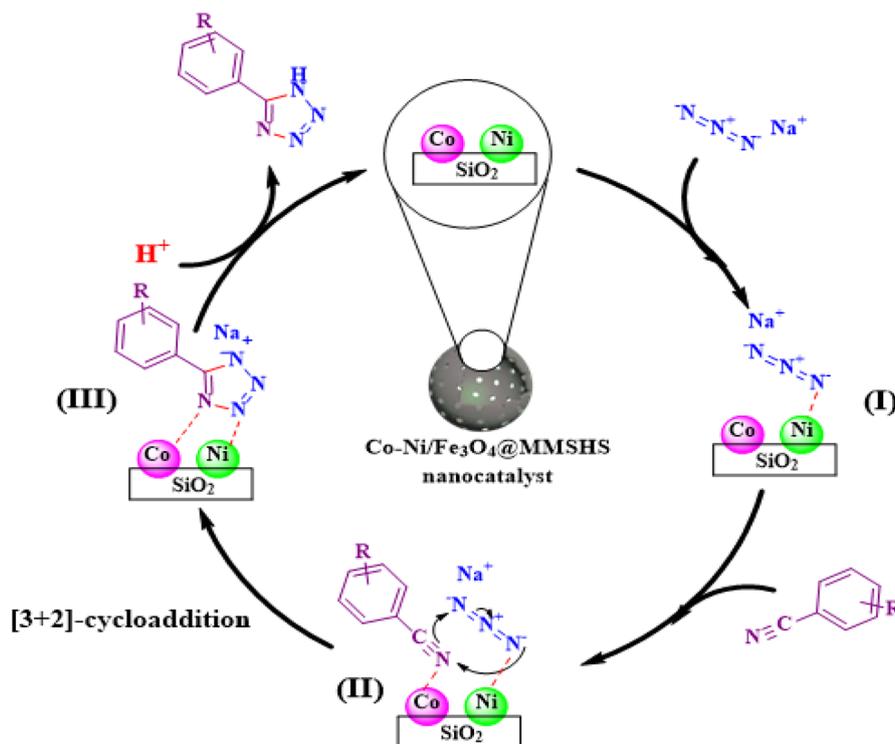
Scheme 2 Proposed reaction mechanism for the synthesis of tetrazole derivatives from sodium azide and aromatic nitriles.

Fig. 12 The reusability results of the Co–Ni/Fe$_3$O$_4$@MMSHS nanocatalyst under the model reaction.

demonstrates its excellent durability and retention of catalytic activity under the reaction conditions. Also, by comparing the catalyst's XRD patterns before and after recovery and examining the data obtained from the reaction yield, it can be concluded that the catalyst's active sites have largely maintained their structure and efficiency after several stages of recovery.

The designed catalyst was also evaluated through a leaching test. The model reaction was placed under optimal conditions for 6 min, and then the catalyst was separated from the reaction medium by an external magnet. After removing the catalyst from the reaction environment, the progress of the reaction was assessed using the TLC technique. The TLC technique revealed that the reaction did not proceed. Stopping the reaction at this stage indicates the stability of the catalyst and its excellent separation ability.
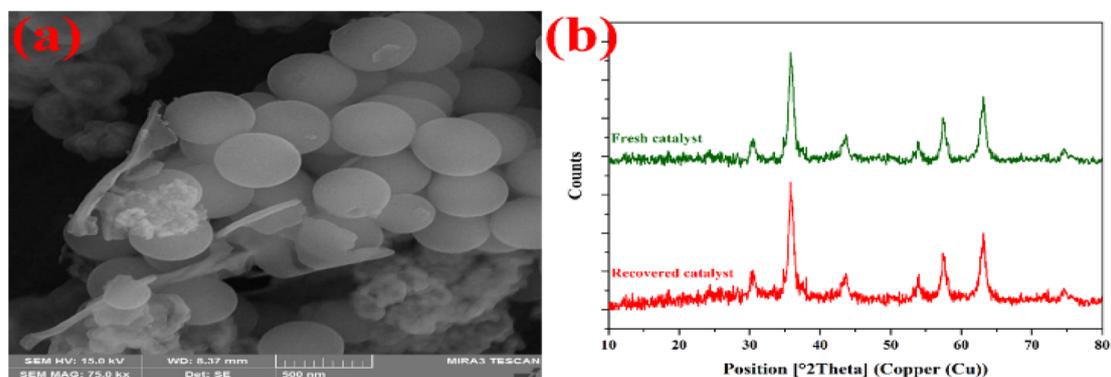

Fig. 13 The FE-SEM image (a) and the XRD spectra (b) of the Co–Ni/Fe$_3$O$_4$@MMSHS nanocatalyst after recovery.

4. Conclusion

The designed catalyst has shown very good performance in synthesizing tetrazole derivatives. This catalyst has reduced the reaction time and enhanced the reaction yield in an environmentally friendly solution. Also, the magnetic property of this catalyst has caused easy separation from the reaction medium. The unique ability to recover and reuse this catalyst has made it one of the most efficient catalysts known for synthesizing tetrazole derivatives. The main goal of this research was to design, prepare, and characterize a catalyst with a large active surface area that can take advantage of the synergistic properties of nickel and cobalt metals to increase reaction efficiency. The spherical and hollow structure with mesopore walls has greatly improved this catalyst's active surface. Using a neutral and non-toxic silica substrate to stabilize nanoparticles has made the catalyst environmentally friendly.

The prepared catalyst showed greater efficiency than other catalysts used in tetrazole synthesis. Many of the catalysts used in synthesizing tetrazoles could not easily separate from the reaction medium, and their efficiency was significantly reduced after reuse. However, the catalyst developed in this research demonstrates effective separation and high recovery capability without compromising efficiency.

Data availability

The data supporting this article have been included as part of the ESI.†

Conflicts of interest

The authors of this paper declare that they have no competing financial interests or personal relationships that could influence their work.

Acknowledgements

References

1 T. Kitanosono, K. Masuda, P. Xu and S. Kobayashi, *Chem. Rev.*, 2018, **118**, 679–746.
2 X. Zhang, X. Yan, J. Guo, Z. Liu, D. Jiang, Q. He, H. Wei, H. Gu, H. A. Colorado, X. Zhang, S. Wei and Z. Guo, *J. Mater. Chem. C*, 2015, **3**, 162–176.
3 A. Eslami and H. Naeimi, *New J. Chem.*, 2024, **48**, 16510–16517.
4 H. Hassanpour and H. Naeimi, *Appl. Organomet. Chem.*, 2024, **38**, e7406.
5 H. Hassanpour and H. Naeimi, *RSC Adv.*, 2024, **14**, 17296–17305.
6 F. Yang, L. Chi, Z. Ye and L. Gong, *J. Am. Chem. Soc.*, 2025, **147**(2), 1767–1780.
7 J.-H. Chen, Q.-J. Yao, M.-Y. Zhong, T.-Y. Jiang, F.-R. Huang, X. Li and B.-F. Shi, *ACS Cent. Sci.*, 2025, **11**(1), 127–135.
8 Z. Ren, J. Lou, J. Huang, F. Wang, H. Chen, Z. Yu, H. Long, J. Gao, H. Zhang and C. Tang, *Sep. Purif. Technol.*, 2025, **358**, 130333.
9 J. Long, L. Ye, H. Peng and Z. Tian, *Chem. Eng. Sci.*, 2025, **301**, 120733.
10 S. Yang, H. Li, M. Zhang, J. Gao, Z. Qi, S. Zhang, W. Li and S. Li, *Appl. Catal. B Environ. Energy*, 2025, **361**, 124621.
11 R. Xiao, D. Ji, L. Wu, Z. Fang, Y. Guo and W. Hao, *J. Colloid Interface Sci.*, 2025, **679**, 566–577.
12 T. Stephen Livingston, P. Madhu, C. Sowmya Dhanalakshmi and R. Vignesh Kumar, *Fuel*, 2025, **379**, 133092.
13 Y. Wu, J. He, K. Zhong, S. Wang, X. Zhu, X. She, W. Jiang, H. Li and H. Xu, *Sep. Purif. Technol.*, 2025, **354**, 128399.
14 F. Yan, X. Zhang, D. Li, N. Zhu and H. Bao, *Appl. Organomet. Chem.*, 2025, **39**, e7932.
15 C. A. Busacca, D. R. Fandrick, J. J. Song and C. H. Senanayake, *Adv. Synth. Catal.*, 2011, **353**, 1825–1864.
16 O. E. Medina, A. A. Amell, D. López and A. Santamaría, *Renew. Sustain. Energy Rev.*, 2025, **207**, 114926.
17 L. Jia, J. Liu, H. Cheng, Z. Zhao and J. Liu, *J. Environ. Sci.*, 2025, **150**, 451–465.
18 S. Zhao, Q. Song, L. Liu, J. Li and D. Zhao, *Energy Convers. Manag.*, 2024, **301**, 118048.
19 Q. Peng, J. Ye and Z. Kang, *Energy*, 2024, **290**, 130152.
20 A. H. Ghasemi and H. Naeimi, *New J. Chem.*, 2020, **44**, 5056–5063.
21 S. Kermanizadeh and H. Naeimi, *Appl. Organomet. Chem.*, 2023, **37**, e7038.
22 M. Bahmanziyari and H. Naeimi, *New J. Chem.*, 2025, **49**, 865–876.
23 S. Kazempour and H. Naeimi, *New J. Chem.*, 2023, **47**, 412–420.
24 S. Kazempour and H. Naeimi, *ChemistryOpen*, 2023, **12**, e202300053.
25 M. Taheri, H. Naeimi and A. H. Ghasemi, *RSC Adv.*, 2023, **13**, 3623–3634.
26 S. Mousavi, H. Naeimi, A. H. Ghasemi and S. Kermanizadeh, *Sci. Rep.*, 2023, **13**, 10840.
27 G. Prieto, H. Tüysüz, N. Duyckaerts, J. Knossalla, G.-H. Wang and F. Schüth, *Chem. Rev.*, 2016, **116**, 14056–14119.
28 W. Zhu, Z. Chen, Y. Pan, R. Dai, Y. Wu, Z. Zhuang, D. Wang, Q. Peng, C. Chen and Y. Li, *Adv. Mater.*, 2019, **31**, 1800426.
29 S. Mohammadi and H. Naeimi, *Appl. Catal., A*, 2020, **602**, 117720.
30 F. Zhang, Y. Wei, X. Wu, H. Jiang, W. Wang and H. Li, *J. Am. Chem. Soc.*, 2014, **136**, 13963–13966.
31 M. H. Zahir, K. Irshad, A. Islam, M. N. Shaikh and M. M. Hossain, *J. Energy Storage*, 2025, **105**, 114679.
32 Z. Hu, X. Yang, Y. Zhang, Z. Sun, W. Liu, G. Pan, H. Wang and M. Sun, *J. Alloys Compd.*, 2025, **1010**, 177110.
33 B. Peng, F. S. Mohammed, X. Tang, J. Liu, K. N. Sheth and J. Zhou, *Bioact. Mater.*, 2025, **43**, 145–161.
34 S. R. Khan, S. Ali, K. Zulfiqar, S. Jamil, S. Noreen, A. Raza and M. J. Latif, *Inorg. Chem. Commun.*, 2025, **172**, 113690.

35 D. K. Kim, J. B. Park, C. Choi and D.-W. Kim, *Chem. Eng. J.*, 2024, **479**, 147820.

36 M. Zhang, X. Zhou, J. Zhong, S. Mo, M. Fu, P. Chen and D. Ye, *Sep. Purif. Technol.*, 2025, **352**, 128171.

37 M. Nasrollahzadeh, Z. Nezafat, N. S. S. Bidgoli and N. Shafiei, *Mol. Catal.*, 2021, **513**, 111788.

38 A. Babu and A. Sinha, *ACS Omega*, 2024, **9**, 21626–21636.

39 M. Atarod, J. Safari and H. Tebyanian, *Synth. Commun.*, 2020, **50**, 1993–2006.

40 B. Agrahari, S. Layek, R. Ganguly and D. D. Pathak, *New J. Chem.*, 2018, **42**, 13754–13762.

41 H. Marishetty Nanjundaswamy and H. Abrahamse, *Heterocycles*, 2014, **89**, 2137.

42 J. Chrétien, G. Kerric, F. Zammattio, N. Galland, M. Paris, J. Quintard and E. Le Grognec, *Adv. Synth. Catal.*, 2019, **361**, 747–757.

43 S. Paudel, X. Min, S. Acharya, D. B. Khadka, G. Yoon, K.-M. Kim and S. H. Cheon, *Bioorg. Med. Chem.*, 2017, **25**, 5278–5289.

44 H. M. Nanjundaswamy and H. Abrahamse, *Heterocycles an Int. J. Rev. Commun. Heterocycl. Chem.*, 2014, **89**, 2137–2150.

45 H. Sharghi, S. Ebrahimpourmoghaddam and M. M. Doroodmand, *J. Organomet. Chem.*, 2013, **738**, 41–48.

46 L. V Myznikov, S. V Vorona, T. V Artamonova and Y. E. Zevatskii, *Russ. J. Gen. Chem.*, 2017, **87**, 731–738.

47 H.-Y. Chen, C.-T. Chen and C.-T. Chen, *Macromolecules*, 2010, **43**, 3613–3623.

48 B. Tahmasbi, P. Moradi, F. Mohammadi, Y. Abbasi Tyula and T. Kikhavani, *Appl. Organomet. Chem.*, 2025, **39**, e7791.

49 Y. A. Tyula, P. Moradi and M. Nikoorazm, *ChemistrySelect*, 2023, **8**, e202301674.

50 B. Agrahari, S. Layek, R. Ganguly and D. D. Pathak, *New J. Chem.*, 2018, **42**, 13754–13762.

51 M. A. E. A. A. A. El-Remaily and O. M. Elhady, *Appl. Organomet. Chem.*, 2019, **33**(11), e4989.

52 H. Sharghi, S. Ebrahimpourmoghaddam and M. M. Doroodmand, *J. Organomet. Chem.*, 2013, **738**, 41–48.